

# Gold Nanoparticles as a Matrix for Visible-Wavelength Single-Particle Matrix-Assisted Laser Desorption/Ionization Mass Spectrometry of Small Biomolecules

Matthew T. Spencer,<sup>†</sup> Hiroshi Furutani,<sup>†</sup> Steven J. Oldenburg,<sup>‡</sup> Thomas K. Darlington,<sup>‡</sup> and Kimberly A. Prather<sup>\*,†</sup>

Department of Chemistry and Biochemistry, University of California at San Diego, La Jolla, California 92093-0314, and nanoComposix Inc., San Diego, California 92111

Received: August 20, 2007; In Final Form: January 2, 2008

Gold nanoparticles (GNPs) are used as the matrix for visible-wavelength matrix-assisted laser desorption/ionization (VIS-MALDI) of individual aerosol particles containing  $\sim 50$  attomole of a small peptide. A dual polarity time-of-flight mass spectrometer was used to obtain both positive and negative ion mass spectra simultaneously from individual particles using a tunable wavelength desorption/ionization laser. The wavelength of the laser was changed from  $\lambda = 440$  to 680 nm to observe the wavelength dependence of analyte ion formation. Detection of the positive sodiated molecular ions and negative deprotonated molecular ion of a small peptide was only possible using 5-nm GNPs and not with larger sized (19- and 44-nm) GNPs. While the masses of gold within the sample particles were similar, surface areas were about 10 times more in the 5-nm GNPs, suggesting the total surface area of GNPs within the sample particles may play a role in the formation of molecular ions. At wavelengths near the peak plasmon resonance of the GNPs ( $\lambda = 500$ –540 nm), negative molecular ion signals from a small peptide was higher than with desorption/ionization at  $\lambda = 440$  nm, with increased fragmentation observed at  $\lambda = 440$  nm. At wavelengths longer than the peak plasmon absorption, the ability to generate a detectable ion signal decreased rapidly, which is consistent with the steep decrease in the absorbance of GNPs by surface plasmon resonance at these wavelengths. Silver nanoparticles, which also exhibit a surface plasmon resonance, were tested and under our conditions did not appear to work as well. The presented results demonstrate that noble metal nanoparticle matrices can be used for on-line VIS-MALDI analysis of small molecular weight species such as peptides or sugars.

## 1. Introduction

In the late 1980s, matrix-assisted laser desorption ionization mass spectrometry (MALDI-MS) emerged as a favorable technique for the mass analysis of high molecular weight analytes (proteins and polymers).<sup>1,2</sup> The success of the MALDI-MS technique is based on using a matrix compound that strongly absorbs the pulsed laser radiation causing effective desorption of analyte imbedded in the matrix into the gas phase, facilitating the soft ionization of analyte molecules.<sup>3</sup> The vast majority of MALDI-MS that is performed today utilizes an ultraviolet (UV) laser such as nitrogen ( $\lambda = 337$  nm) or frequency-tripled Nd:YAG ( $\lambda = 355$  nm) to irradiate a sample embedded in a UV-absorbing matrix.<sup>3</sup> IR lasers such as CO<sub>2</sub> ( $\lambda = 10.6$   $\mu$ m) or Er:YAG ( $\lambda = 2.94$   $\mu$ m) with IR-absorbing matrices such as glycerol are also used.<sup>4,5</sup> The majority of highly successful matrices are small organic acids such as 3,5-dimethoxy-4-hydroxycinnamic acid or 2,5-dihydroxybenzoic acid. Although these acid matrices work well for the analysis of large polymers or proteins, the extensive fragmentation of the matrix materials can cause considerable interference in the low mass range of the mass spectrum. This has been a major limitation for using conventional MALDI-MS as a tool in small molecule analysis; although even with this limitation, the technique is still used in small molecule analysis to some degree.<sup>6</sup>

Inorganic nanoparticles/rods/tubes and inorganic surfaces of various compositions have also been pursued as a matrix for MALDI with some success.<sup>2,7–18</sup> These matrices circumvent the problem of interference in the low mass range by avoiding the use of an organic matrix and many have been used in small molecule analysis.<sup>7,13–15,17,18</sup> Of particular interest are matrices comprised of noble metal nanoparticles. A unique characteristic of gold and silver nanoparticles is that they exhibit a surface plasmon resonance (SPR) at visible wavelengths. The SPR is responsible for the deep red color of gold nanoparticles (GNPs) and the yellow color of silver nanoparticles in solution.<sup>19,20</sup> One of the advantages of using noble metal nanoparticles such as GNPs as a matrix is the absence of severe fragmentation of matrix materials.<sup>18,21–24</sup> It was shown that the reduced fragmentation of the GNP matrix allowed for the effective analysis of small molecules (MW < 600) in UV-MALDI.<sup>18,21–24</sup> As suggested by Chen et al. (2007) and Furutani et al. (2007), the SPR in the visible wavelength region opens the possibility for noble metal nanostructures to be used as matrices for visible wavelength MALDI (VIS-MALDI).

VIS-MALDI may offer advantages over traditional UV-MALDI for the analysis of some organic molecules, such as those that absorb in the UV region and thus are susceptible to fragmentation using UV-MALDI. The majority of small organic molecules do not absorb in the visible wavelength range and therefore are less likely to undergo fragmentation by direct absorption of visible wavelength radiation. However, there are relatively few reports on VIS-MALDI mass spectrometry due

\* To whom correspondence should be addressed. Phone: (858) 822-5312. Fax: (858) 534-7042. E-mail: kprather@ucsd.edu.

<sup>†</sup> University of California at San Diego.

<sup>‡</sup> nanoComposix Inc.

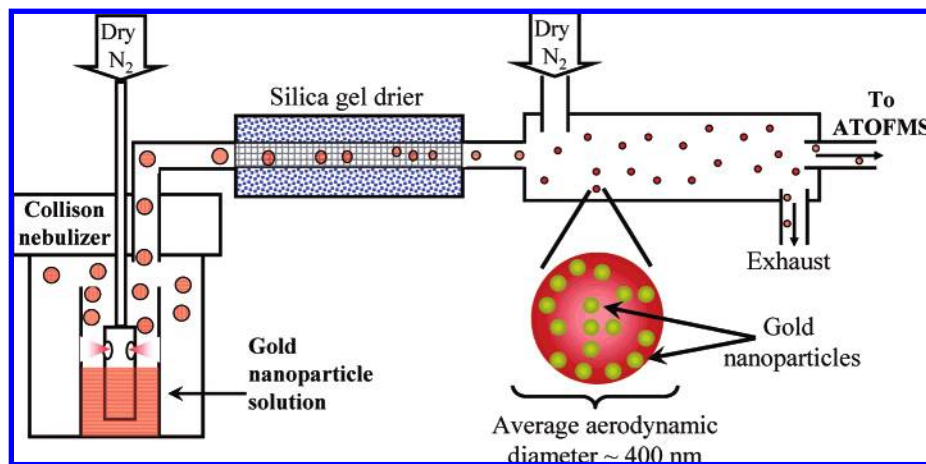


**Figure 1.** Diagram of the method used for generating aerosol particles containing metal nanoparticles and analyte molecules used for on-line VIS-MALDI analysis.

to the limited number of suitable matrices which absorb visible wavelength light. Organic dyes, graphite surfaces, and inorganic nanoparticles/rods are a few matrices that have been employed for VIS-MALDI.<sup>10,15,16,25–28</sup> However, in most cases, there are still limitations of using the matrix for small molecule analysis due to the large number of fragment matrix ions in the low mass region.

In this research, GNPs are used as the matrix for single particle VIS-MALDI mass spectrometry. Utilizing a GNP matrix for VIS-MALDI offers several benefits. For example, the GNP matrix has been shown to produce less fragment ions particularly in the low mass range using UV-MALDI.<sup>17,18</sup> Furthermore, the SPR of the particles can be tuned from the visible to near-infrared wavelengths by modifying the shape and/or structure of the nanoparticle.<sup>29–32</sup> This tunability is not obtainable with ordinary organic matrices because the absorption spectra are intrinsic to the individual matrix molecules. By tuning the optimal resonance of the GNP matrix to a wavelength that is optimally coupled to a visible wavelength laser, a high performance and cost-effective VIS-MALDI methodology can be established. It has also been shown that SPR excitation enhances the local electromagnetic fields by orders of magnitude resulting in ultrahighly sensitive optical spectroscopy.<sup>33,34</sup> Such enhancement by the SPR may also assist further improvement in the detection of organic molecules via mass spectrometry.

Herein, we discuss the analysis of small quantities of organic molecules ( $\sim 50$  attomole) in individual aerosol particles using GNPs as a matrix for on-line VIS-MALDI using a single particle dual polarity time-of-flight mass spectrometer. The single particle mass spectrometer used in this work offers the unique ability of obtaining both positive and negative polarity mass spectra simultaneously which is not possible with conventional MALDI instruments. This gives us the advantage of being able to perform on-line MALDI and to compare changes in the positive and negative ions generated from every laser shot directly. GNPs of different sizes are evaluated to examine the effect of GNP size on analyte signal intensities. The wavelength of the LDI laser is varied from  $\lambda = 440\text{--}680$  nm to understand the effect of SPR on the VIS-MALDI process. A brief discussion of several possible applications using the GNP VIS-MALDI technique and the potential for using other noble metal nanoparticles as a VIS-MALDI matrix are also presented.

## 2. Experimental Section

**2.1. Sample Preparation.** GNPs were fabricated by nanoComposix Inc. (San Diego, CA) using a previously established

method.<sup>35</sup> The 5-nm gold particles were washed two times to remove impurities using ultracentrifugation followed by removal of the supernatant and resuspension of the gold pellet using milli-Q water. Silver nanoparticles were also fabricated by nanoComposix Inc. using a base-catalyzed reduction of silver nitrate. Particle sizes were determined using transmission electron microscopy. GNP stock solutions contained  $5 \pm 2$  nm ( $2.3 \times 10^{15}$  particles/mL),  $19 \pm 3$  nm ( $8.3 \times 10^{11}$  particles/mL), or  $44 \pm 8$  nm ( $6.28 \times 10^{10}$  particles/mL) diameter GNPs. For experiments using silver nanoparticles,  $14 \pm 7$  nm particles were used ( $\sim 8.3 \times 10^{12}$  particles/mL).

All reagents were obtained commercially and used without further purification. Stock solutions of  $\text{NH}_2$ -tryptophan-glycine-glycine- $\text{CO}_2\text{H}$  (WGG) peptide ( $\sim 3$  mg/mL) and the sugars D-ribose and L-arabinose ( $\sim 2$  M) were prepared using milli-Q purified water, stored at  $4^\circ\text{C}$ , and used within 24 h of preparation. An aliquot of peptide or sugar stock solution was pipetted into  $\sim 10$  mL of metal nanoparticle solution. Solutions containing 5-nm gold particles were prepared by diluting  $\sim 50$   $\mu\text{L}$  of gold stock solution into  $\sim 10$  mL of milli-Q purified water. Solutions containing 19-nm gold particles were prepared by diluting  $\sim 1.5$  mL of gold stock solution into  $\sim 10$  mL of milli-Q purified water. Solutions containing 44-nm gold particles were prepared by diluting  $\sim 2.0$  mL of gold stock solution into  $\sim 10$  mL of milli-Q purified water. Silver nanoparticle (14 nm) solution was prepared by diluting  $\sim 500$   $\mu\text{L}$  silver stock solution into 10 mL milli-Q purified water.

Figure 1 shows the process used for aerosolizing and drying particles containing the matrix (metal nanoparticles) and analyte. Particles were generated by nebulizing the metal nanoparticle solutions using a Collision type nebulizer operated at a flow rate of 1.5–1.7 lpm. The aerosol stream from the nebulizer was passed through a diffusion dryer which consists of a Pyrex flow tube (50 cm length  $\times$  6 cm inside diameter (i.d.)) with a coaxial stainless steel fine mesh tube (50 cm length  $\times$  1 cm i.d.) on the inside. The space between these coaxial tubes was filled with silica gel which dries the aerosols as they flow through the inner mesh tube. After passing through the diffusion drier, the aerosol stream was diluted with  $\sim 1.0$  lpm of dry nitrogen as it entered a second flow tube (100 cm length  $\times$  5 cm inside diameter). The relative humidity at the exit of this flow tube was  $<15\%$ . A 0.08-lpm flow of the dried aerosol particles was then drawn into the single particle mass spectrometer for VIS-MALDI analysis.

**2.2. Single-Particle MALDI-MS.** It should be noted that there is a significant difference between a conventional MALDI

mass spectrometer and the aerosol time-of-flight mass spectrometer (ATOFMS) used in these experiments. In a conventional MALDI, samples are deposited on a metal plate that is placed into the mass spectrometer; a laser then desorbs and ionizes a fraction of the sample from this metal target. By use of an ATOFMS, sample aerosol particles are analyzed on-line, which involves desorbing and ionizing individual particles composed of the analyte and matrix as they enter the source region of a dual ion time-of-flight mass spectrometer.

A detailed description of the ATOFMS has been given elsewhere, and only a brief description is given here.<sup>36–39</sup> Particle charges are neutralized before particles enter the ATOFMS using Polonium-210 neutralizer to prevent deflection of charged particles within the electric field of the ion source region. Particles enter the ATOFMS through an aerodynamic lens that collimates the particles into a tightly focused beam.<sup>38,40,41</sup> At the exit of the aerodynamic lens ( $10^{-3}$  Torr), the incoming gas undergoes a supersonic expansion that causes any associated particles to accelerate to terminal velocities that are dictated by the vacuum aerodynamic sizes of the particles. Particles then enter a light-scattering region where they pass through two vertically separated (6 cm) continuous wave (CW) Nd:YAG lasers operated at 532 nm. These lasers are used to measure the particle velocity, which can be ultimately correlated with the particle aerodynamic diameter. Information on the particle velocity and position within the system is then used to calculate the appropriate time to fire a third Q-switched Nd:YAG laser for desorption and ionization of the particle at the precise time when they enter the ion source region of the mass spectrometer. The laser power for each analyzed particle was saved using a J25LP-2 probe attached to an EPM1000 power meter (Molelectron, USA). By use of this method, ATOFMS yields a vacuum aerodynamic diameter and a positive and negative ion mass spectrum for each individual particle.

A wavelength tunable laser ( $\lambda = 410\text{--}680$  nm) consisting of a Quantel Brilliant Q-switched Nd:YAG laser operated at 355 nm and OPOTEK Magic Prism optical parametric oscillator (OPO) was used for desorption/ionization of particles. The spot size of the laser in the source region of the mass spectrometer was  $\sim 0.8$  mm. Changing the wavelength of the laser system caused small changes in the position of the output laser spot. Small movements of the laser spot position in the source region can cause changes in the detected ion intensity and the mass calibration. Therefore significant care was taken to ensure that the laser spot position in the source region could be kept constant as the wavelength of the laser was adjusted. This was accomplished by passing the laser through two apertures separated by  $\sim 2$  meters and projecting the laser spot at the exit of the mass spectrometer on a fixed position  $\sim 3$  meters away. A Continuum Minilite II, Q-switched Nd:YAG laser operated at 532 nm was also used as a desorption/ionization laser in some experiments.

**2.3. Data Analysis.** Mass spectra were imported into a database in Matlab (The MathWorks, Inc.) and analyzed using portions of the YAADA toolkit [http://www.yaada.org]. Within Matlab, a group of individual particle mass spectra can be averaged together creating an average mass spectrum (AM).

### 3. Results and Discussion

**3.1. Properties of Sample Particles.** Table 1 shows the measured and calculated physical characteristics of the individual sample particles that contained the WGG peptide and 5-nm GNPs. The average vacuum aerodynamic diameter of sample particles was measured as  $\sim 400$  nm. By use of the

**TABLE 1: Physical Characteristics of the Aerosol Particles That Contain 5-nm GNPs and the WGG Peptide**

property	value
average particle aerodynamic diameter	400 nm
estimate of gold–WGG composite density	$1.38\text{ g}\cdot\text{cm}^{-3}$
average physical diameter	290 nm
volume percent of gold	$\sim 1.0\%$
volume percent of WGG	$\sim 99.0\%$
no. 5-nm GNPs per particle	$\sim 2000$
moles of WGG per particle	$\sim 50$ attomole

concentration of GNPs and WGG peptide in solution, the volume fraction of gold and WGG peptides in an individual sample particle is estimated to be  $\sim 1$  and  $99\%$ , respectively. We assume the density of the WGG peptide is similar to that of other small peptides,  $\sim 1.2\text{ g}\cdot\text{cm}^{-3}$ , and that the ratio of gold to WGG in a dried particle is the same as in solution. From the calculated volume fraction, a composite density ( $\rho_p$ ) for a dried WGG–GNP sample particle is estimated to be  $\sim 1.38\text{ g}\cdot\text{cm}^{-3}$  using eq 1

$$\text{composite density} = (\text{gold density} \times \text{gold volume fraction}) + (\text{peptide density} \times \text{peptide volume fraction}) \quad (1)$$

The measured vacuum aerodynamic diameter ( $d_a$ ) can be converted to a physical diameter ( $d_p$ ) using the composite density and is calculated to be  $\sim 290$  nm using eq 2<sup>42</sup>

$$d_a = d_p \left( \frac{\rho_p}{\rho_0} \right)^{1/2} \quad (2)$$

By use of the physical diameter, the volume fractions of gold and WGG peptide leads to an estimate of approximately 2000 GNPs and 50 attomole of WGG peptide per 290 nm sample particle. This estimate was made using the average GNP diameter measured with a TEM.

**3.2. Aerosol Particle Mass Spectra.** Parts a and b of Figure 2 show a positive polarity AM from single sample particles that contained only GNPs (denoted as “pure gold”) and an AM from single sample particles that contained GNPs and WGG (gold–WGG). Parts c and d of Figure 2 show the corresponding negative polarity AM. The data shown in Figure 2 were generated using 540-nm laser radiation for desorption/ionization. It should be noted that no mass spectra could be generated from pure WGG sample particles (particles containing no GNPs) under the current experimental conditions; that is, the presence of GNPs was required for ion formation.

Sample particles containing GNPs without analyte (Figure 2a) show positive ion peaks for gold at  $^{197}\text{Au}^+$  and  $^{394}\text{Au}_2^+$ . Also peaks at  $89^+$  ( $\text{C}_2\text{H}_2\text{O}_2\text{P}$ ),  $105^+$  ( $\text{C}_3\text{H}_6\text{O}_2\text{P}$ ), and  $109^+$  ( $\text{C}_3\text{H}_{10}\text{O}_2\text{P}$ ) are detected and most likely from the fragmentation of tetrakis(hydroxymethyl)-phosphonium chloride (THPC,  $\text{C}_4\text{H}_{12}\text{O}_4\text{P}$ ), which is used during the fabrication of the GNPs and was not completely removed during the purification of the GNPs. The chemical assignments of the THPC fragments are given as likely suggestions and are not definitive as there are other chemical assignments that could give rise to similar  $m/z$  values. For comparison, Figure 2b shows the positive ion AM for particles containing GNPs and WGG. This AM contains peaks for gold ( $^{197}\text{Au}^+$  and  $^{394}\text{Au}_2^+$ ), sodium adducts of WGG ( $341\text{MNa}^+$  and  $364\text{MNa}_2^+$ ), and fragments of WGG at  $130^+$  and  $160^+$ . The fragment at  $m/z +130$  is most likely the methylene indole fragment of tryptophan, which is the dominant fragmentation channel for photon ionization or electron impact of tryptophan.<sup>43</sup> The fragment at  $m/z +160$  is likely a Gly–



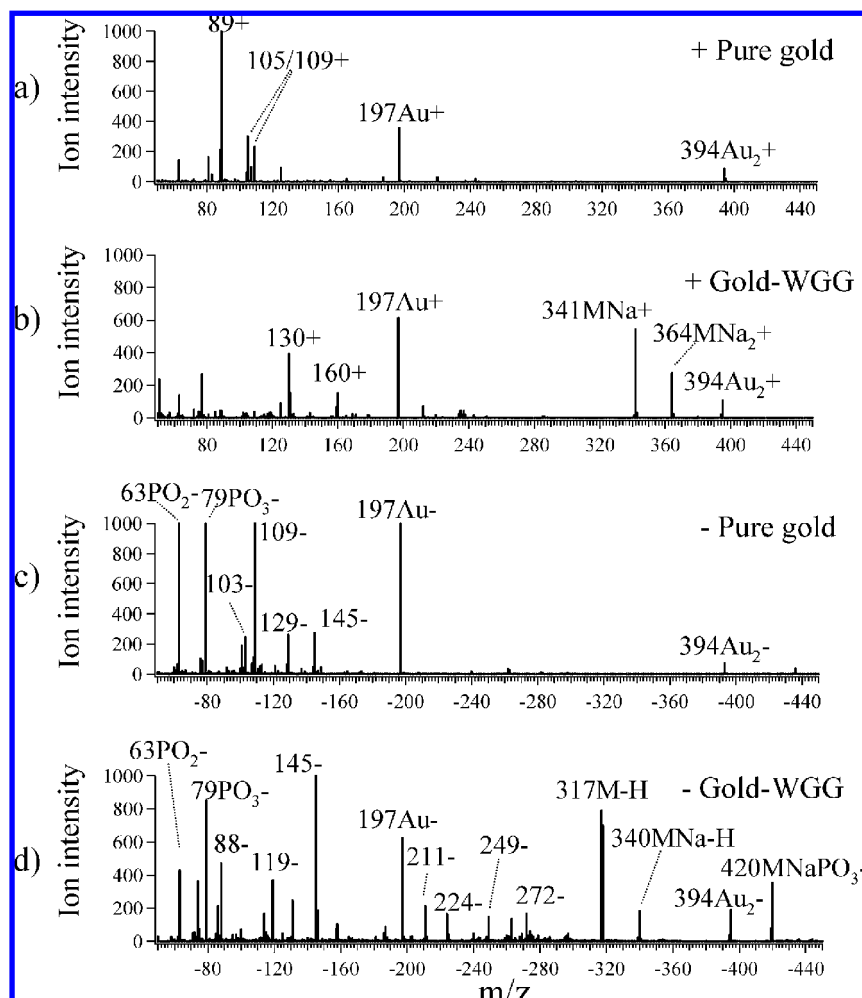


**Figure 2.** Positive average mass spectra are shown for aerosol particles containing (a) only GNPs (pure gold) and (b) both GNPs and the small peptide, WGG. Panels c and d show the corresponding negative polarity average mass spectra. The spectra were generated using a 540-nm desorption/ionization laser.

Gly containing fragment ion ( $C_5H_8N_2O_4^+$ ) because  $m/z$  +160 is not a common fragment of Trp. Formation of the sodium adduct molecular ions with GNP matrix using VIS-LDI laser is quite similar to those observed with GNP matrix using UV-MALDI.<sup>18</sup> The ions 89+, 105+, and 109+ that appeared in the pure GNPs are not present in the sample containing WGG. We observed that the presence of these ions depended on the concentration of analyte. At low analyte concentrations, these ions were still present but decreased as analyte concentration increased. This is possibly caused by the addition of compounds (WGG, Na, etc.) that are more easily ionized than the THPC fragments. When analytes (WGG, Na, sugars, etc.) are added to the GNPs, they have concentrations in excess of the residual THPC. Therefore, during the ionization process there are many more gas phase analyte molecules which compete for the limited pool of electrons and become negative ions compared to the THPC.

The negative ion AM for pure GNPs is shown in Figure 2c and contains peaks for gold ( $^{197}Au^-$  and  $^{394}Au_2^-$ ), phosphate ( $63PO_2^-$  and  $79PO_3^-$ ), and other ions at 103-, 109-, 129-, and 145-. Again, the phosphate and "other ions" are likely from residual THPC left over after fabrication and purification of GNPs. Figure 2d shows that the negative ion AM for GNPs with WGG contain peaks for gold ( $^{197}Au^-$  and  $^{394}Au_2^-$ ), phosphate ( $63PO_2^-$  and  $79PO_3^-$ ), deprotonated WGG ( $317M-H$ ), deprotonated sodium adduct WGG ( $340MNa-H$ ), sodium phosphate adduct WGG ( $420MNaPO_3^-$ ), ions that were present

in the gold blank (129- and 145-), and ions presumably from the fragmentation of the WGG peptide at 211-, 224-, 249-, and 272-. The negative ion fragments are more difficult to assign as they have been far less studied in the literature. The larger negative ion fragments we observe are not the same as the fragmentations observed for tryptophan using electron impact.<sup>44</sup> A significant amount of the negative ion fragments can arise from complex dissociation reactions associated with multiple bond cleavages and electronic/structural rearrangements that makes any chemical assignments extremely speculative from this dataset alone. The observed negative ion fragments most likely have undergone rearrangements and are a combination of Trp-Gly-Gly peptide. Figure 2 clearly demonstrates that GNPs can act as a VIS-MALDI matrix for the analysis of small peptides using single particle mass spectrometry and give little interference in the low mass range in the 150 and 400  $m/z$  window.

**3.3. Effect of GNP Size.** Measurements using different sizes of GNPs were made to determine the effect of GNP size on the analyte ion signals. Figure 3a shows a waterfall plot of the positive ion AM for samples containing similar amounts of the peptide WGG but differently sized GNPs (5, 19, and 44 nm). Figure 3b shows the corresponding negative ion AMs obtained using 532-nm laser radiation for desorption/ionization.

Of the three GNP sizes that were used, only sample particles containing 5-nm GNPs generated a detectable amount of WGG molecular ions ( $^{341}MNa^+$ ,  $^{364}MNa_2^+$ ,  $^{317}M-H$ ,  $^{340}MNa-H$ ,

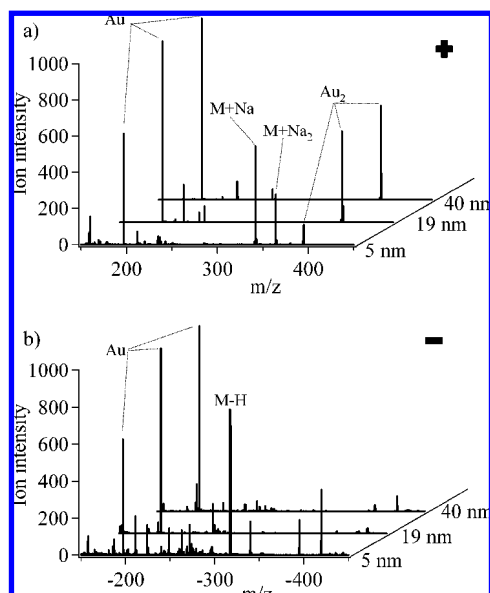


**Figure 3.** Average mass spectra that were generated from aerosol particles that contained different sizes of GNPs are stacked and offset for comparison. The positive ion spectrum is shown in (a) and negative ion spectrum in (b). Laser radiation at 532 nm was used for desorption/ionization.

and  $^{420}\text{MNaPO}_3^-$ ). No detectable signal from the peptide was observed even after increasing the amount of WGG by more than 5 times in the experiments with the larger 19 and 44 nm GNPs. McLean et al. (2005) observed similar results and noted that the GNP matrix did not produce any detectable peptide ions in the negative ion mode using GNPs larger than 10 nm as a matrix for UV-MALDI (positive ions were detected).<sup>9</sup> Wen et al. (2007) also observed an increase in analyte ion signal for 30 nm vs 50 nm using silicon based nanoparticles as the UV-MALDI matrix.<sup>13</sup>

The mass of gold in a sample aerosol particle is estimated to be  $2.5 \times 10^{-15}$ ,  $2.0 \times 10^{-15}$ , and  $2.0 \times 10^{-15}$  g for the sample particles with 5, 19, and 44 nm GNPs respectively, meaning a similar mass of gold was present in all sample particles for the different sizes of GNP. This estimate is based on the GNP size and concentrations given in the methods section and average aerosol diameters of 290, 320, and 300 nm for the 5, 14, and 44 nm experiments, respectively. On the other hand, the total surface area of GNPs within the differently sized particles was different and estimated to be  $1.5 \times 10^5$ ,  $3.2 \times 10^4$ , and  $1.4 \times 10^4$  nm<sup>2</sup> for 5, 19, and 44 nm GNP, respectively. This represents about an order of magnitude difference in the surface area between sample particles containing the 5, 19, and 44 nm GNPs. Thus, surface area of gold could be an important factor for the formation of analyte ions in these experiments. The melting temperature of GNPs has been shown to dramatically decrease as particle size decreases.<sup>45</sup> Also, as nanoparticle size increases, the extinction coefficient becomes less weighted by absorption and more weighted by scattering. The different melting temperatures and absorption efficiencies of GNPs at different sizes could also be important parameters influencing the formation of analyte ions. Experiments using a more refined set of GNPs with sizes between 2 and 19 nm and also gold nanoshells will be used in a future study to quantify how mass and surface area of gold affect the ion signals and to find the optimum GNP size for MALDI experiments.

**3.4. Effect of LDI Laser Wavelength and Power.** Figure 4a shows the percentage of particles that generated a mass spectrum (hit percent) vs different LDI wavelengths (laser power

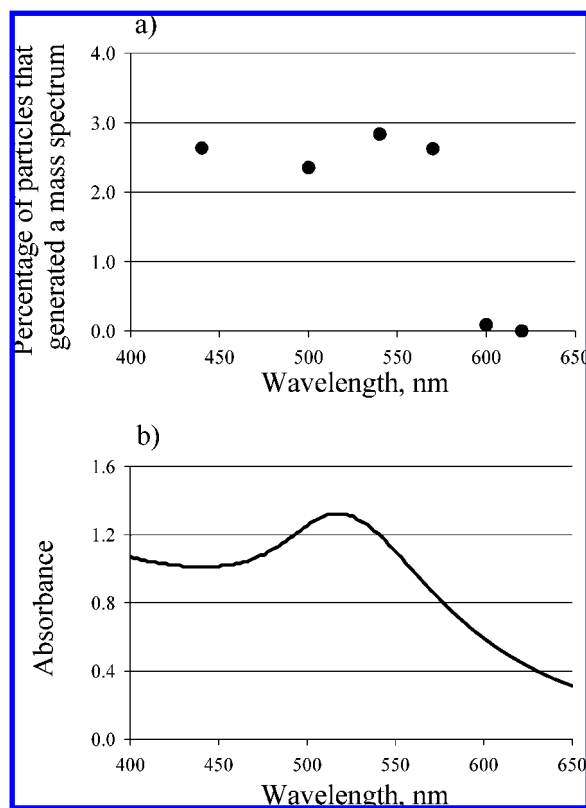


**Figure 4.** The hit percent (i.e., percentages of particles that were detected with the tracking/sizing lasers and generated a mass spectrum) are plotted vs the LDI wavelength in (a). The absorbance of a solution of ~5-nm GNPs vs wavelength is shown in (b).

≈ 1.2 mJ/pulse) with WGG peptides and 5-nm GNPs. The hit percent is a metric for how effectively particles are desorbed and ionized at different wavelengths in single-particle mass spectrometry. Because no experimental parameters were changed except for the wavelength of the LDI laser, the hit percent uniquely reflects the physicochemical property of the sample particles at a given wavelength. The hit percent is fairly constant (~3%) from 440 to 570 nm and then rapidly drops to almost zero at 600 nm. No mass spectra could be generated at 620 nm. This overall trend is the same at laser powers other than 1.2 mJ/pulse. However, at higher powers the hit percentage is generally higher, and at lower powers the hit percentage is generally lower. This is expected because higher laser powers lead to the formation of detectable ion signal more frequently than at lower laser powers. The wavelength dependence of the hit percentage is quite consistent with the wavelength dependence of optical absorption of GNP. Figure 4b shows the absorption spectrum of 5-nm GNP at the stock concentration. The peak of the SPR absorption centered at  $\lambda = 520$  nm overlays the tailing edge of the atomic absorption of gold at shorter wavelengths and drops steeply at wavelengths longer than the peak SPR. Similar wavelength dependences between the hit percentages and the absorption spectra of the GNPs clearly indicate that SPR plays a role in VIS-LDI detection of analyte ions.

Parts a and b of Figure 5 show the laser wavelength and power dependence of the ion peak area for the sodiated WGG ion peak  $[\text{M} + \text{Na}]^+$  and the peak area for the deprotonated WGG ion  $[\text{M} - \text{H}]^-$  at different laser powers (0.4 mJ laser power bin widths). The vertical error bars represent twice the standard deviation in the measured areas. Interestingly, the  $[\text{M} + \text{Na}]^+$  ion peak area (see Figure 5a) remains fairly constant with increasing laser powers at wavelengths of 500 and 540 nm,

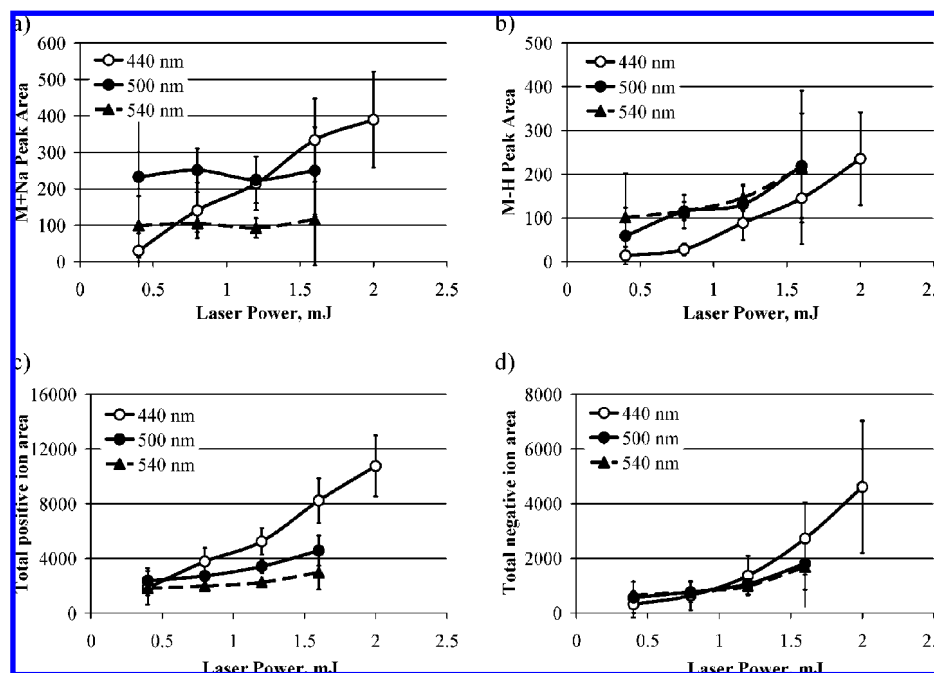


**Figure 5.** Peak areas are plotted vs laser power for different desorption/ionization wavelengths for (a) sodiated WGG ion ( $M + Na$ )<sup>+</sup>, (b) deprotonated WGG ion ( $M - H$ )<sup>-</sup>, (c) total sum of positive ion peak areas, and (d) total sum of negative ion peak areas. The spectra were generated using the 5-nm GNP matrix.

which are near the peak plasmon absorption of the GNPs (520 nm, see Figure 4b). Such a dependence on laser power was only observed for  $[M + Na]^+$  with 500- and 540-nm LDI laser wavelengths. In contrast, as laser power increased, 440-nm LDI laser irradiation yielded more  $[M + Na]^+$  ion and reached even larger intensity at the higher laser power conditions over the other wavelengths. However, under the lowest laser power conditions, the 500-nm LDI laser irradiation yielded the largest peak area. The  $[M - H]^-$  peak area increased with laser power for all LDI wavelength conditions although the  $[M - H]^-$  peak area at 440 nm is consistently less than at 500- and 540-nm wavelengths (Figure 5b). Although different mechanisms such as surface desorption, layer by layer evaporation, volume ablation by phase explosion, and volume ablation by laser induce pressure pulses have been suggested for UV-MALDI,<sup>3</sup> at this stage we cannot explain the desorption/ionization mechanisms that might be occurring at the different visible wavelengths; however, current results suggest that a different LDI mechanism is occurring when the laser wavelength occurs at or near the SPR vs the LDI mechanism at shorter laser wavelengths (e.g.,  $\lambda = 440$  nm) based on the observed distinct ion patterns.

In general, more fragment ions and increased total ion yields are expected using higher laser power conditions. Parts c and d of Figure 5 are consistent with this and show the total positive and negative ion area (sum for all  $m/z$ ) steadily increases with increasing laser power. Parts c and d of Figure 5 also show that the total ion peak area is generally highest at 440 nm and lower at 500 and 540 nm for a given laser power. This is presumably due to the higher energy per photon at shorter wavelengths, which leads to both the creation of more overall ions as well as more fragmentation. Figure 6 shows a series of positive ion area matrices for different LDI wavelengths (average laser power  $\approx 1.6$  mJ/pulse). Although the major mass spectral features are similar among the different LDI wavelengths, there are less fragment ions (circled by the dashed line) as the LDI wavelength becomes longer. Figures 5 and 6 clearly demonstrate that lower laser powers and a laser wavelength resonant to SPR absorption ( $\lambda \approx 520$  nm) generate more intense

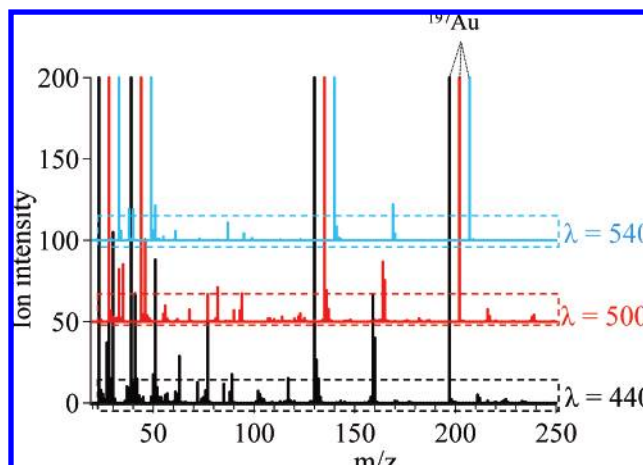


**Figure 6.** Stacked plots of the average mass spectrum generated from particles ionized at  $\lambda = 440$ , 500, and 540 nm. The dashed box around the fragment ions is shown to draw attention to the decreasing fragments as  $\lambda$  increases.

quasimolecular ion  $[M + Na]^+$  and  $[M - H]^-$  species with less fragmentation than excitation at an off-resonant condition ( $\lambda = 440$  nm).

**3.5. Analysis of Sugars.** The GNP matrix described thus far has been shown to assist the VIS-LDI of a small peptide prior to mass spectrometric analysis. The technique is also tested for the analysis of sugars. Figure 7 shows the positive and negative ion AM for samples containing the 5-nm GNP matrix with D-ribose and L-arabinose (stereoisomeric sugars) using a Q-switched frequency doubled Nd:YAG laser ( $\lambda = 532$  nm). Similar to the detection of the WGG peptide using VIS-MALDI, incorporating the GNP as a matrix was essential for detection; i.e., no mass spectrum of the pure sugars could be obtained without the GNPs. The positive ion AM for each sugar has the same molecular/fragment ions with very similar intensities and both appear almost identical. The positive ion similarities includes the sodiated molecular ion ( $173MNa^+$ ), THPC fragment ions ( $89^+$ ,  $105^+$ ,  $109^+$ ), and a sugar fragment  $73^+$

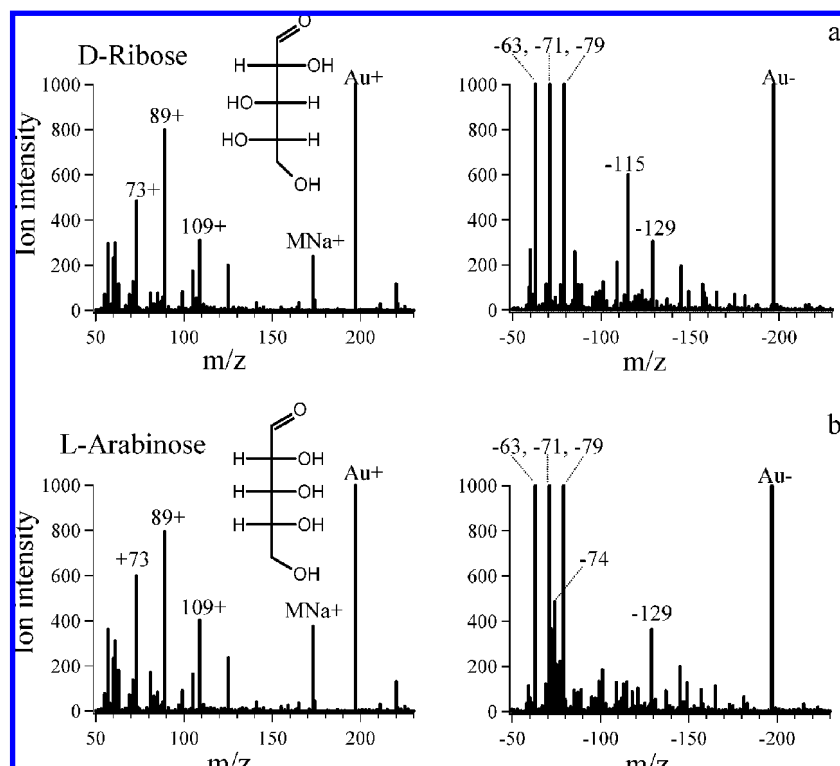


**Figure 7.** The positive and negative polarity average mass spectra are shown that were generated from aerosol particles containing a 5-nm GNP matrix and the sugar (a) D-ribose or (b) L-arabinose.

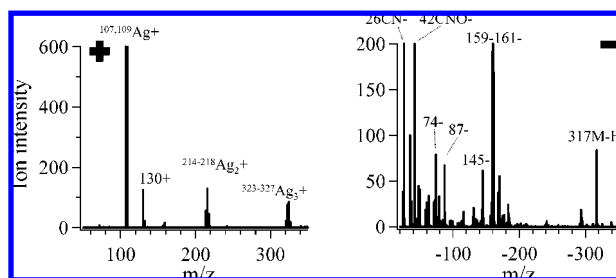


**Figure 8.** Positive and negative ion average mass spectra from aerosol particles containing 14-nm silver nanoparticles and WGG. Aerosol particles were desorbed and ionized using 540-nm laser radiation.

( $C_3H_5O_2^+$ ). Although the positive ion AMs are similar, there are unique differences in the negative ion AM for each sugar. D-Ribose has a significant peak at  $m/z$  -115, while L-arabinose does not. L-Arabinose has an ion peak at  $m/z$  -74, while D-ribose does not. The ribose/arabinose negative ion fragments observed here are not the same as electron attachment fragmentation patterns for ribose.<sup>46</sup> Because of the detailed fragmentation mechanisms that can give rise to these negative ions, significantly more research will need to be done to definitively determine the chemical assignments of these fragments. Regardless, these unique negative fragment ion patterns could potentially be used to differentiate between these two isomers. This result demonstrates that the VIS-MALDI technique with GNP matrix can also be applied to the analysis of other small molecules including sugars.

**3.6. VIS-MALDI Using Other Metal Particle Matrices.** Other noble metal nanoparticles could also possibly serve as a matrix for VIS-MALDI. Because spherical silver nanoparticles also have a plasmon absorption in the visible wavelength region (maximum at  $\lambda \approx 440$  nm), we tested a 14-nm silver nanoparticle (SNP) matrix with the WGG analyte. Figure 8 shows the positive and negative ion AM from particles containing SNPs and WGG peptide using laser radiation at a wavelength of 540

nm. The WGG peptide concentration was calculated to be similar to the experiments with GNPs and the average dried sample particle contained  $\sim 120$  SNPs. The positive ion spectrum contains only 4 significant peaks; three peaks are attributed to silver and silver cluster ions ( $Ag^+$ ,  $Ag_2^+$ ,  $Ag_3^+$ ), and an additional peak occurs at  $m/z$  130+. There was no appreciable amount of WGG molecular ion present in the positive polarity mass spectra; however  $m/z$  130+ is likely the methylene indole fragment of tryptophan because this peak was not observed in SNP control experiments. It may be possible that smaller SNPs may improve its overall performance as a VIS-MALDI matrix making it similar to the results obtained for GNPs. However further experiments are necessary to test this. Unfortunately, at the time of these experiments, smaller SNPs were unavailable.

The negative ion mass spectra did however show a relatively intense peak attributed to the deprotonated WGG molecular ion at  $m/z$  -317 ( $M - H^-$ ). There are also fragment ions at  $m/z$  26-, 42-, 74-, 87-, 145-, 159-, 160-, and 161-, which were not present in silver nanoparticle control experiments and are therefore attributed to fragments of the WGG analyte. Many of the negative ion fragments are different than those observed using the GNP matrix. We do not attempt to give chemical assignments to these fragment ions due to the complex processes by which they can form. The amount of fragmentation using the SNP matrix appears to be more significant than with the 5-nm GNP matrix experiments.

Desorption/ionization using an LDI wavelength near the peak plasmon absorption of the SNPs ( $\lambda = 440$  nm) generated positive ion mass spectra with similar features (peaks and intensity) to  $\lambda = 540$  nm; however significantly less overall negative ion intensities were observed (data not shown). Further experiments using silver nanoparticles are necessary to understand this result. Although the 5-nm gold appears to facilitate the VIS-LDI process better than the 14-nm SNP matrix, it remains unclear whether silver nanoparticles would enhance this



process more or less. It is possible that 5-nm SNPs would show similar results to GNP; however they were unavailable at the time of these experiments.

An attempt was also made to use titanium oxide particles as a matrix for the VIS-MALDI technique. Titanium oxide particles have no SPR and little absorption in the visible wavelength range. As expected, no mass spectra were obtainable with a titanium oxide particle matrix at wavelengths ranging between 440 and 640 nm using laser powers similar to the experiments with gold and silver (<3.0 mJ/pulse). This is further evidence that, for noble metal nanostructures, the plasmon absorbance in the visible wavelength region is promoting the VIS-MALDI process.

#### 4. Conclusion

This study demonstrates that the plasmon absorption of GNPs can be used to facilitate the VIS-LDI of small peptide and sugar molecules from individual aerosol particles. Experiments using different sizes of GNPs at the same gold mass loading densities suggest that the surface area of gold is an important factor that affects analyte ion intensities; increased surface area equates with obtaining an increased analyte ion signal. Desorption/ionization near the maximum plasmon absorption of the GNP yields more intense negative polarity analyte ion signal than at shorter wavelengths. Furthermore, less analyte fragmentation was observed in mass spectra at wavelengths near the peak SPR vs shorter wavelengths. The technique has been shown to be useful for small molecule characterization by producing little interferences in the small mass window compared to standard organic matrices. Silver nanoparticles, which also have a visible wavelength SPR, also appear to facilitate the visible wavelength laser desorption/ionization process.

**Acknowledgment.** We would like to thank Professor Judy Kim and Diana Schlamadinger from the Department of Chemistry and Biochemistry at the University of California, San Diego, for providing the tunable wavelength laser and assisting with its calibration and operating procedures.

#### References and Notes

- (1) Karas, M.; Hillenkamp, F. *Anal. Chem.* **1988**, *60*, 2299.
- (2) Tanaka, K.; Waki, H.; Ido, Y.; Akita, S.; Yoshida, Y.; Yohida, T. *Rapid Commun. Mass Spectrom.* **1988**, *2*, 151.
- (3) Dreisewerd, K. *Chem. Rev.* **2003**, *103*, 395.
- (4) Overberg, A.; Karas, M.; Bahr, U.; Kaufmann, R.; Hillenkamp, F. *Rapid Commun. Mass Spectrom.* **1990**, *4*, 293.
- (5) Overberg, A.; Karas, M.; Hillenkamp, F. *Rapid Commun. Mass Spectrom.* **1991**, *5*, 128.
- (6) Cohen, L. H.; Gusev, A. I. *Anal. Bioanal. Chem.* **2002**, *373*, 571.
- (7) Kinumi, T.; Saisu, T.; Takayama, M.; Niwa, H. *J. Mass Spectrom.* **2000**, *35*, 417.
- (8) Kirk, J. S.; Bohn, P. W. *J. Am. Chem. Soc.* **2004**, *126*, 5920.
- (9) McLean, J. A.; Stumpo, K. A.; Russell, D. H. *J. Am. Chem. Soc.* **2005**, *127*, 5304.
- (10) Schurenberg, M.; Dreisewerd, K.; Hillenkamp, F. *Anal. Chem.* **1999**, *71*, 221.
- (11) Sunner, J.; Dratz, E.; Chen, Y. C. *Anal. Chem.* **1995**, *67*, 4335.
- (12) Ugarov, M. V.; Egan, T.; Khabashesku, D. V.; Schultz, J. A.; Peng, H. Q.; Khabashesku, V. N.; Furutani, H.; Prather, K. S.; Wang, H. W. J.; Jackson, S. N.; Woods, A. S. *Anal. Chem.* **2004**, *76*, 6734.
- (13) Wen, X. J.; Dagan, S.; Wysocki, V. H. *Anal. Chem.* **2007**, *79*, 434.
- (14) Wei, J.; Buriak, J. M.; Siuzdak, G. *Nature* **1999**, *399*, 243.
- (15) Chen, L. C.; Ueda, T.; Sagisaka, M.; Hori, H.; Hiraoka, K. *J. Phys. Chem. C* **2007**, *111*, 2409.
- (16) Chen, L. C.; Yonehama, J.; Ueda, T.; Hori, H.; Hiraoka, K. *J. Mass Spectrom.* **2007**, *42*, 346.
- (17) Furutani, H.; Oldenburg, S. J.; Aluwihare, L.; Prather, K. A. *Anal. Chem.* Submitted.
- (18) Furutani, H.; Oldenburg, S. J.; Prather, K. A. *Anal. Chem.* Submitted.
- (19) Kreibitz, U.; Genzel, L. *Surf. Sci.* **1985**, *156*, 678.
- (20) Link, S.; El-Sayed, M. A. *Int. Rev. Phys. Chem.* **2000**, *19*, 409.
- (21) Lee, K. H.; Chiang, C. K.; Lin, Z. H.; Chang, H. T. *Rapid Commun. Mass Spectrom.* **2007**, *21*, 2023.
- (22) Huang, Y. F.; Chang, H. T. *Anal. Chem.* **2007**, *79*, 4852.
- (23) Su, C. L.; Tseng, W. L. *Anal. Chem.* **2007**, *79*, 1626.
- (24) Huang, Y. F.; Chang, H. T. *Anal. Chem.* **2006**, *78*, 1485.
- (25) Cornett, D. S.; Duncan, M. A.; Amster, I. J. *Anal. Chem.* **1993**, *65*, 2608.
- (26) Kim, J.; Paek, K.; Kang, W. *Bull. Korean Chem. Soc.* **2002**, *23*, 315.
- (27) Smith, C. J.; Chang, S. Y.; Yeung, E. S. *J. Mass Spectrom.* **1995**, *30*, 1765.
- (28) Tang, K.; Allman, S. L.; Jones, R. B.; Chen, C. H. *Org. Mass Spectrom.* **1992**, *27*, 1389.
- (29) Sun, Y. G.; Xia, Y. N. *Analyst* **2003**, *128*, 686.
- (30) Kelly, K. L.; Coronado, E.; Zhao, L. L.; Schatz, G. C. *J. Phys. Chem. B* **2003**, *107*, 668.
- (31) Oldenburg, S. J.; Averitt, R. D.; Westcott, S. L.; Halas, N. J. *Chem. Phys. Lett.* **1998**, *288*, 243.
- (32) Kamat, P. V. *J. Phys. Chem. B* **2002**, *106*, 7729.
- (33) Barnes, W. L.; Dereux, A.; Ebbesen, T. W. *Nature* **2003**, *424*, 824.
- (34) Otto, A.; Mrozek, I.; Grabhorn, H.; Akemann, W. *J. Phys.: Condens. Matter* **1992**, *4*, 1143.
- (35) Duff, D. G.; Baiker, A.; Edwards, P. P. *Langmuir* **1993**, *9*, 2301.
- (36) Gard, E.; Mayer, J. E.; Morrical, B. D.; Dienes, T.; Fergenson, D. P.; Prather, K. A. *Anal. Chem.* **1997**, *69*, 4083.
- (37) Prather, K. A.; Nordmeyer, T.; Salt, K. *Anal. Chem.* **1994**, *66*, 1403.
- (38) Su, Y.; Sipin, M. F.; Furutani, H.; Prather, K. A. *Anal. Chem.* **2004**, *76*, 712.
- (39) Holecck, J. C.; Denkenberger, K. A.; Mayer, J. E.; Moffet, R. C.; Poon, G.; Sanchez, R. O.; Rebotier, T.; Furutani, H.; Su, Y.; Guazzotti, S.; Prather, K. A. *Anal. Chem.* **2007**. Manuscript in preparation.
- (40) Liu, P.; Ziemann, P. J.; Kittelson, D. B.; McMurry, P. H. *Aerosol Sci. Technol.* **1995**, *22*, 314.
- (41) Liu, P.; Ziemann, P. J.; Kittelson, D. B.; McMurry, P. H. *Aerosol Sci. Technol.* **1995**, *22*, 293.
- (42) DeCarlo, P. F.; Slowik, J. G.; Worsnop, D. R.; Davidovits, P.; Jimenez, J. L. *Aerosol Sci. Technol.* **2004**, *38*, 1185.
- (43) Zhan, Q.; Wright, S. J.; Zenobi, R. *J. Am. Soc. Mass Spectrom.* **1997**, *8*, 525.
- (44) Abdoul-Carime, H.; Gohlke, S.; Illenberger, E. *Chem. Phys. Letters* **2005**, *402*, 497.
- (45) Dick, K.; Dhanasekaran, T.; Zhang, Z. Y.; Meisel, D. *J. Am. Chem. Soc.* **2002**, *124*, 2312.
- (46) Bald, I.; Kopyra, J.; Illenberger, E. *Angew. Chem., Int. Ed.* **2006**, *45*, 4851.